Silicon Nitride Induces Osteoconduction Via Activated Mitochondrial Oxidative Phosphorylation and Neovascularization

Wayne Gonzales [1], Ronit Khade [1], Takeru Kondo [1,2], Satomi Arimoto [1,3], Taro Inagaki [1,3], Akishige Hokugo [1,3], Karolina Elżbieta Kaczor-Urbanowicz [4,5], Bryan McEntire [6], Ryan Bock [6], Takahiro Ogawa [1], Giuseppe Pezzotti [7,8], Ichiro Nishimura [1,4]*

[1] Weintraub Center for Reconstructive Biotechnology, Section of Prosthodontics, UCLA School of Dentistry, Los Angeles, CA, USA 90095

[2] Department of Molecular & Regenerative Prosthodontics, Tohoku University Graduate School of Dentistry, Sendai, Japan 980-8575

[3] Regenerative Bioengineering and Repair Laboratory, Division of Plastic and Reconstructive Surgery, Department of Surgery, David Geffen School of Medicine at UCLA, Los Angeles, CA, USA 90095

[4] Section of Biosystems and Function, UCLA School of Dentistry, Los Angeles, CA, USA 90095

[5] Section of Orthodontics, UCLA School of Dentistry, Los Angeles, CA, USA 90095

[6] SINTX Technologies, Salt Lake City, UT, USA 84119

[7] Ceramic Physics Laboratory, Kyoto Institute of Technology, Sakyo-ku, Matsugasaki, Kyoto, Japan 606-8585

[8] Department of Molecular Genetics, Institute of Biomedical Science, Kansai Medical University, 2-5-1 Shinmachi, Hirakata, Osaka, Japan 573-1010

Short title: Osteoconductive Silicon Nitride Implant

* Corresponding Author

Ichiro Nishimura, DDS, DMSc, DMD

Weintraub Center for Reconstructive Biotechnology

UCLA School of Dentistry, Box 951668, CHS B3-087, Los Angeles, CA 90095 USA

Email: inishimura@dentistry.ucla.edu FAX: +1 (310) 825-6345

Abstract

Silicon Nitride (Si_3N_4: SiN) is a thermodynamically stable ceramic material with excellent mechanical properties and wear/corrosion resistance for industrial applications. SiN is also proposed for orthopedic and dental implant applications because of its enhanced osteoconduction. However, the biological mechanism of SiN-induced bone formation has not been fully elucidated. In this study, SiN significantly increased *in vitro* mineralization of human bone marrow mesenchymal stromal cells (BM-MSC) and *in vivo* peri-implant bone volume in mouse femurs over conventionally used titanium (Ti) implants. RNA sequencing of BM-MSC cultured on SiN disc revealed that the functional gene clusters associated with mitochondrial oxidative phosphorylation were significantly elevated over the Ti disc groups. SiN in aqueous solution releases ammonium/ammonia, which may provide a source for glutamine-dependent energy production. It was confirmed that BM-MSC upregulated the glutamate-ammonia ligase (*GLUL*) expression with osteogenic condition. In addition, SiN increased the expression of functional gene clusters involving vascular formation. The upregulation of *HIF1a in vitro* and the increased VEGFR3-positive blanching vascular structures *in vivo* supported that SiN-induced neovascularization. This study has uncovered an important mechanism that SiN stimulates osteoconduction through unique glutamine-driven mitochondrial oxidative phosphorylation and establishes oxygen and nutrient supply by neovascularization, leading to stable osseointegration. (197 words)

Keywords: Silicon nitride, Osteoconduction, Osseointegration, RNA sequencing, Mitochondria oxidative phosphorylation, Neovascularization

1. Introduction

Increasingly aging societies worldwide require the continuous productivity by senior population that will need repair, regeneration, or replacement of diseased body parts. For example, the incidence of osteoarthritis, rheumatoid arthritis, and traumatic arthritis increases with age [1, 2], which reflects the recent increase in the utilization of prosthetic hip and knee surgery among US Medicare beneficiaries [3]. By contrast, dental implant usage is spread across age groups. However, in those 60 years or older, a larger number of dental implants were placed [4]. This treatment trend is consistent with increasing tooth loss with advancing age. In fact, 17.3% of seniors 65 years and older in the US have no remaining teeth (https://www.cdc.gov/oralhealth/publications/OHSR-2019-index.html).

Cementless prosthetic hip and knee implants and dental implants achieve mechanical stability into the host bone bed through osseointegration [5, 6]. Osseointegration was initially thought to be induced on the surface of bio-inert materials such as titanium (Ti). However, it has been found that bone responses are modulated on surface-modified Ti materials [7, 8] and zirconia (Zr) ceramic materials [9, 10] suggesting that osseointegration is a material-driven biological process. As such there is a novel opportunity to identify new biomaterials that can improve implant osseointegration for deteriorated host bone tissue of aging patients.

Any load-bearing implant material requires mechanical stability. Silicon Nitride (Si_3N_4: SiN) is an industrial ceramic material with outstanding thermodynamic stability and currently used to make highly durable components in the automotive, aviation and aerospace industries. SiN exhibits mechanical strength, toughness, and wear and corrosion resistance; properties that are also suitable for biomedical implants (**Table 1**) [11].

To date, SiN is known to have biocompatible and osteoconductive properties. SiN discs [12] as well as SiN-coated Ti [13], polyetherketoneketone [14], and polyetheretherketone [15, 16] discs were shown to increase *in vitro* bone formation of various osteogenic cells over

conventional implant materials. These studies suggest that SiN has an enhanced osteoconductivity, although the biological mechanisms are not yet fully understood.

The objective of the present study was to compare SiN with other commonly used implant materials, using an *in vitro* culture model and an *in vivo* mouse femur implant model. To elucidate the SiN-induced biological mechanism, RNA sequencing analysis was used to generate new hypotheses that were validated in subsequent *in vitro* and *in vivo* experiments. The outcome of this study shows that the osteoconductive effect of SiN is manifested through novel mechanisms that activate glutamine-driven mitochondrial oxidative phosphorylation providing the energy necessary for new bone formation, and that induce neovascularization activity ensuring oxygen and nutrient supply for further bone maturation.

2. Results:

2.1. In vitro evaluation of SiN, MTi, ATi and Zr discs (Figure 1A)

The surface of ceramic SiN and Zr discs presented the characteristic crystallin nano structures, whereas metallic MTi and ATi discs presented anisotropic and isotropic surfaces, respectively (**Figure 1B**). The surface roughness measurements indicated that SiN and Zr discs presented similar Sa, Sz and Sdr values, whereas ATi discs showed the highest values and MTi discs showed the lowest values (**Figure 1C**). The θ angle measurement was similar among the disc samples that were hydrophilic but not superhydrophilic (**Figure 1D**).

Human bone marrow mesenchymal stromal cells (BM-MSC) cultured on SiN, MTi, ATi and Zr discs attached to the material surface and developed stress fibers (**Figure 1E**). The cell growth measured by Wst-1 assay did not show the major differences among the disc groups, although SiN disc appeared to slow the cell proliferation rate (**Figure 2A**). The striking observation, however, was the robust increase in Alizarin red S staining of BM-MSC cultured on SiN disc for 21 days, which was significantly higher that other groups (**Figure 2B**).

2.2. Gene expression analysis

The total RNA samples from BMSC cultured on SiN, MTi, ATi and Zr discs for 7 days and 14 days were isolated for RT-PCR. The steady state expression of osteogenic differentiation-related genes such as Runx family transcription factor 2 (*RUNX2*), alkaline phosphate (*ALP*), osteopontin (*OPN*), alpha 1 type I collagen (*COL1A1*) and osteocalcin (*OCN*) did not show significant differences among the SiN, MTi, ATi and Zr groups (**Figure 2C**), suggesting that BM-MSC used in this study exhibited fate-specific differentiation to osteoblasts and the materials did not affect this process.

A circadian rhythm gene, neuronal PAS domain 2 (*Npas2*), was previously reported in the peri-implant bone associated with Ti materials with micro-rough surfaces [17, 18], and was determined to be indispensable toward achieving the increased osseointegration of the surface roughened Ti implant [19]. In this study, BM-MSC cultured on SiN, ATi and Zr discs demonstrated the increased *Npas2* expression over the MTi group, albeit the statistical significance was reached between the SiN and MTi groups (**Figure 2C**).

To investigate the molecular and cellular mechanism of increased *in vitro* mineralization by SiN disc, the total RNA samples from the SiN, MTi and ATi groups were subjected to RNA sequencing. The transcriptome data were analyzed for differentially expressed and co-regulated genes. Gene ontology (molecular function and cellular component) as well as KEGG (Kyoto Encyclopedia of Genes and Genomes) pathways; indicated that SiN material enriched the gene clusters involved in mitochondrial oxidative stress and oxidative phosphorylation over MTi and ATi materials (**Figure 3A**).

2.3. Surface chemistry of SiN

It has been reported that SiN in aqueous solution releases nitrogen ions, which interact with water molecules to form ammonium/ammonia [20, 21]. Furthermore, SiN-derived ammonia was postulated to form nitric oxide (NO) due to the presence of free electrons formed from splitting of

water molecules [20, 22] (cf. draft and chemical reactions in **Figure 3B**). The formation of NO was also experimentally proved by means of *in situ* fluorescence microscopy [20].

We thus hypothesized that SiN-derived ammonium/ammonia could be a source of glutamine-driven mitochondria oxidative phosphorylation [23] (**Figure 3C**). Among the nutrients such as glucose and fatty acid [24], glutamine provide the efficient substrate for mitochondrial oxidative phosphorylation to generate energy in the form of adenosine triphosphate (ATP) [23]. A pathological depletion of glutamine from bone marrow has been shown to impair osteogenic differentiation of BM-MSC [25]. Glutamine is intracellularly synthesized by glutamine synthetase (glutamate-ammonia ligase, GLUL) (**Figure 3C**) [26]. The RTPCR demonstrated the steady state GLUL expression was significantly increased in BM-MSC cultured in the osteogenic medium for 21 days; however, it was not modulated by biomaterials (**Figure 3D**).

2.4. SiN, MTi and ATi implants in the mouse femur model

Miniature implants (0.8 mm D and 6 mm L) were fabricated from SiN, MTi and ATi (**Figure 4A**) and surgically placed in mouse femurs (**Figure 4B**) following protocols reported previously [27]. After 1 week and 3 weeks of healing, implant osseointegration was measured by the implant push-in test (**Figure 4C**). SiN and ATi implants resisted mechanical loading at the 1-week healing period, generated the push-in value, i.e., the force required to dislodge the implant. The push-in value at the 3-week period increased and the ATi implant exhibited the largest push-in value followed by SiN implant and MTi implant (**Figure 4D**).

The mouse femur specimens containing miniature implants were fixed in 10% buffered formalin and subjected to micro-CT imaging. The 100 μm periphery from the surface of implant embedded in the bone marrow was selected as the region of interest (ROI) (**Figure 5A**) and bone morphometry was measured. The peri-implant bone associated with SiN implant exhibited larger bone volume (BV/TV) and bone surface (BS/TV), and smaller trabecular space (Tb.Sp) as well as more trabecular number (Tb.N) than that of MTi and ATi implants (**Figure 5B**).

Furthermore, the smallest structure model index (SIM) was found in the SiN group, suggesting more laminar structure of its per-implant bone (**Figure 5B**).

After micro-CT imaging, the mouse femur samples were decalcified, and the longitudinal histological sections were made after the removal of implant. The long and continuous peri-implant bone was observed in the SiN group, whereas the peri-implant bone of the MTi and ATi groups was less frequent or fragmented, respectively (**Figure 6A**). It was noted that the bone marrow around MTi implant was associated with the increased adipose tissue. The peri-implant bone surface to form bone-to-implant contact (BIC) showed periodically spaced connective tissue structures in the SiN group (**Figure 6B**). By contrast, BIC surfaces of MTi and ATi implants were relatively smooth. A thin layer of nuclei was found to cover the peri-implant bone surface toward the MTi implant (**Figure 6B**), which was not included in the BIC ration measurement. The BIC ratio was largest in the SiN group, followed by the ATi group and the MTi group (**Figure 6C**). The thickness of the peri-implant bone significantly varied; however, the mean thickness was widest in the SiN group (**Figure 6D**), supporting the micro-CT outcome.

2.5. SiN induced angiogenesis

Next, the RNA sequence data of BM-MSC cultured on SiN, MTi and ATi discs were reanalyzed by Biological Pathway gene ontogeny revealed that SiN stimulated “Extracellular matrix organization” and “Extracellular structure organization” genes (**Figure 7A**) and, in particular, type VI collagen genes were upregulated. Furthermore, a large segment of the top 20 biological pathways was related to angiogenesis such as blood vessel morphogenesis and vasculature development (**Figure 7A**). The signature gene in the angiogenesis biological pathway clusters was hypoxia-inducible factor 1a (*HIF1a*). The significantly increased steady state expression of *HIF1a* was determined by RT-PCR in the BM-MSC cultured on SiN disc as compared to those cultured on MTi and ATi discs (**Figure 7B**).

To validate this RNA sequencing data analysis, immunohistochemistry was performed. The vascular endothelial cell marker CD31 was only faintly positive in bone marrow tissue around SiN implant and not clearly observed in the MTi and ATi group (**Figure 8A**). By contrast, microvasculature-like structures that were positive with VEGF receptor 3 (VEGFR3) were clearly observed in the SiN group and to some extent in the ATi group (**Figure 8B**). The microvasculature structures in the MTi group were negative with VEGFR3. The greater number of VEGFR3 positive microvasculature structure was confirmed in the SiN group than the MTi and ATi group (**Figure 8C**).

3. Discussion:

The present study revealed unique osteoconductive mechanisms that contribute to the osseointegration of SiN implants. Unlike osteoinduction, which involves the recruitment and differentiation of immature cells to pre-osteoblasts, osteoconduction is defined as the stimulation of fate-committed pre-osteoblasts toward bone formation within the bone microenvironment [28]. The present study demonstrated the robust increase of *in vitro* mineralization of human BM-MSC cultured on SiN disc (**Figure 2**), and *in vivo* bone generation around SiN implants in the mouse femur bone marrow (**Figures 5** and **6**).

Biomaterial-induced bone formation has been characterized as upregulation of the selected osteogenic differentiation genes by RT-PCR. However, DNA microarray and more recent RNA sequencing data did not associate the expression of these genes with osteoconduction [29, 30]. Bone formation is an energy consuming biological process and osteoblasts are metabolically active requiring high levels of energy from adenosine triphosphate (ATP) [31, 32]. Mitochondria are cytosolic organelles that uptake glucose-derived molecules, fatty acids, amino acids, and other fuels for oxidative phosphorylation to generate ATP. Targeted deletion of a core subunit composing mitochondrial complex I in mouse skeletal progenitor cells resulted in deficient bone embryogenesis and spontaneous bone fracture [33]. Cyclophilin D knockout mice, a genetic

model of high oxidative metabolism, showed greater osseointegration in the spinal fusion site [34]. The role of implant materials to regulate mitochondrial activity in the peri-implant microenvironment has gained recent attention [35]. In the present study, the functional enrichment analysis of the RNA sequencing data revealed that SiN stimulated the upregulation of mitochondrial oxidative phosphorylation-related gene clusters over MTi and ATi materials (**Figure 3**) whereas osteogenic differentiation-related genes were not modulated by these materials (**Figure 2**).

When SiN (Si_3N_4) is exposed to aqueous solutions, the Si-N covalent bond is cleaved and nitrogen is leached out, it reacts with water molecules, and forms ammonium (NH_4^-) and ammonia (NH_3). Pezzotti (2019) reported that the ratio between ammonium and ammonia released from SiN was sensitive to fluid pH and predominantly ammonium was released under physiological conditions (pH7.4) at the concentration range of 0.01 mMol/dm^3 [20]. While the SiN-released ammonia content is too low to be toxic, ammonium may positively affect the bone marrow cells surrounding SiN implant. Liu et al. (2022) reported that BM-MSC, which highly expressed GLUL in bone marrow, were able to convert ammonium and glutamate to glutamine and to increase proliferation and osteogenic differentiation rates [36]. In fact, glutamine has been identified as a major fuel of nitrogen and carbon for mitochondria oxidative metabolism [37] leading to mitochondrial oxidative phosphorylation and ATP synthesis [23, 38]. Therefore, we postulate that the increased bone formation unique to SiN material may in part be activated by ammonium released from SiN supporting the glutamine-driven mitochondrial oxidative phosphorylation system.

Angiogenesis is critical to supply nutrient and oxygen for new bone formation and maturation [39]. Therefore, bone conductive biomaterials have been designed to induce neovascularization by incorporating vascular endothelial growth factor (VEGF) [40, 41] and arginine-glycine-asparate (RGD) adhesion molecule [42] that target vascular endothelial cells [43, 44]. Recent *in vitro* studies reported that the SiN doped micro-arc oxidation coatings

increased human umbilical vein endothelial cells (HUVEC) migration [13] and silicon oxynitrophosphide (SiOP) coatings increased the tube formation and expression of *HIF1a* by HUVEC [45]. The present study analyzed the RNA sequence data revealed and the upregulated functional gene clusters for vascular system generation in BM-MSC exposed to SiN material (**Figure 7**). We are aware that BM-MSC is not vascular endothelial cells; however, SiN and its released chemical components may have the specific cellular and molecular effects mimicking the vascular formation in BM-MSC.

Because of the cascade of chemical reactions following the release of nitrogen and its successive reaction with water molecules, SiN leads to the formation of NO in aqueous solution [20, 21]. This is known to stimulate angiogenesis [46, 47]. Accordingly, the local environment around SiN implant may stimulate endothelial precursor cells to the vascular formation without the use of VEGF and RGD. In the present immunohistochemistry study identified the increased $CD31^{dim}VEGFR3^{+}$ vascular-like structure in the bone marrow near the SiN implant (**Figure 8**). CD31 is a vascular endothelial cell marker, which is strongly expressed in type H endothelium of metaphysis but less expressed in sinusoidal vessels or type L endothelium of diaphysis [48]. VEGFR3 is present in all endothelial cells during development, and then it becomes restricted to the lymphatic endothelium in the adult [49]. However, VEGFR3 is found in the microvasculature in the wound and supports the growth of sprouting new blood vessels from pre-existing vasculature [50]. Therefore, $CD31^{dim}VEGFR3^{+}$ vascular-like structure was considered the sign of neovascularization induced by SiN implant.

Osseointegration measured by the load resistant push-in test measures the strength of bone-implant bonding [19, 27]. SiN and ATi implants were comparative in establishing the BIC (**Figure 6**), while ATi implant exhibited the larger push-in value than SiN implant (**Figure 4**). This observation may be explained by the mechanical interdigitation to micro-rough surface of ATi implant, although the interface tissue on the implant surface may be differentially modulated

by the micro-rough surface [19] and the discrete nano-crystalline surface modification [51]. The scope of the present study did not investigate this mechanism any further.

Orthopedic and dental implants have been accepted as a reliable treatment with successful long-term survival. However, the clinical success of these elective surgical treatments has been influenced by the selection of subjects with careful exclusion of underlying patient conditions that might negatively affect the outcome, such as diabetes and severe osteoporosis. As such, there is a need for new and improved materials for selected clinical applications. The outcome of the present study suggests that SiN represents a novel implant material exhibiting the increased osteoconductive activity through activation of the mitochondrial oxidative phosphorylation system. Furthermore, the SiN-associated neovascularization may support the maturation and long-term health of integrated bone tissue.

4. **Methods**:

4.1. Ethics statement

All animal procedures were approved by the UCLA Animal Research Committee (ARC #1997-136) and followed the PHS Policy for the Humane Care and Use of Laboratory Animals. All animals had free access to food and water and were maintained in regular housing with a 12-12h light/dark cycle.

4.2. Experimental materials and surface characterizations

For *in vitro* studies, disc samples (12.7 mm diameter, 1 mm thick) were produced using commercially pure Ti (Grade 2, ASTM F67, Vincent Metals, Minneapolis MN, USA), Zr (TZ-3Y, Tosoh USA, Grove City, OH, USA) and SiN (Si_3N_4, SINTX Technologies, Salt Lake City, UT, USA). Ti discs were produced by parting discs from a stock rod with the desired diameter using a lathe and then machining the surfaces of the discs. Zr and SiN samples were produced by pressing of spray-dried powers into compacts, green machining compacts into discs, then firing

the discs to remove organic components and densify the ceramic bodies. Zr was sintered at 1400°C for 2 hr in air to greater than 99% theoretical density in accordance with product literature supplied by Tosoh. SiN, containing 10% total by mass Al_2O_3 and Y_2O_3 sintering aids was sintered and hot isostatically pressed to greater than 99% of theoretical density as described in previous work [52].

For *in vivo* studies, miniature implants (0.8 mm diameter, 6 mm long) were produced in commercially pure Ti and SiN (SINTX Technologies, Salt Lake City, UT). Ti implants were machined directly from stock wire of the desired diameter. Silicon nitride implants were pressed, green machined, and sintered into blanks as described for the disc samples above. Fired blanks were then diamond ground to achieve the final desired geometry.

Ti discs and Ti miniature implants were subjected to the acid-etch protocol using 67% sulfuric acid (Sigma-Aldrich, St. Louis, MO, USUSA) at 115°C for 75 seconds as previously reported [53]. Untreated Ti material was designated as machined Ti (MTi), whereas sulfuric acid-treated Ti material was designated as ATi. All materials were sterilized under UV light for 30 minutes for each surface.

The surface morphology of each material was examined by scanning electron microscopy (SEM: XL30, Philips, Eindhoven, Netherlands) and laser profile microscopy (VK-8500, Keyence, Osaka, Japan). The surface topography was evaluated for average roughness (Sa), peak-to-valley roughness (Sz) and developed interfacial area ratio (Sdr). The wettability of material surface was determined by measuring the contact angle of 3 µl ddH2O.

4.3. Human bone marrow mesenchymal stromal cells (BM-MSC)

Human BM-MSC (iMSCs: Applied Biological Materials, Richmond, BC, Canada) was expanded in Dulbecco's modified Eagle's medium (DMEM; Life Technologies, Grand Island, NY, USA) with 15% fetal bovine serum (FBS; Life Technologies, Grand Island, NY, USA) and 100 U penicillin/0.1 mg/ml streptomycin (Life Technologies) at 37℃, 5% CO_2 in a humidified incubator.

Human BM-MSC from passages 2 to 8 were used in this study. The cells were seeded on the each disc in 24-well culture plates (1×10^5 cells/well) and cultured in osteogenic induction medium consisting of Minimum essential medium Eagle, alpha modification (MEM α; Life Technologies) supplemented with 15% FBS, 0.1 μM dexamethasone (Sigma-Aldrich, Saint Louis, MO, USA), 10 mM β-glycerophosphate (Sigma-Aldrich), 50 μg/ml ascorbic acid (Sigma-Aldrich), and 250 ng/ml amphotericinB (Thermo Fisher Scientific, Waltham, MA, USA). The culture medium was changed every 3 days.

After 7 days of osteogenic induction, the human BM-MSC attached to the discs were transferred into the other new 24-well culture plate. The cells were incubated in 10% WST-1 reagent (Thermo Fisher Scientific) with the osteogenic induction medium for 1 h. The supernatant was placed in a 96-well plate and absorbance was measured at 405 nm using a microplate reader.

After 21 days of osteogenic induction, the human BM-MSC were fixed with 10% formalin neutral buffer solution (Thermo Fisher Scientific) and immersed in 40 mM alizarin red S (Sigma-Aldrich) solution (pH 4.1) for 20 minutes with gentle shaking, followed by washing with distilled water. To quantify the staining results, 10% acetic acid (Sigma-Aldrich) was added to each well, and the plate was incubated at room temperature for 30 minutes with shaking. The loosely attached cells were scraped in acetic acid, transferred to microcentrifuge tubes and vortexed for 30 seconds. Samples were heated at 85°C for 10 minutes, followed by cooling on ice for 5 minutes. After centrifugation at 20,000 *g* for 15 minutes, 10% ammonium hydroxide (Thermo Fisher Scientific) was added. Finally, the supernatant was placed in a 96-well plate and absorbance was measured at 405 nm using a microplate reader.

4.4. Osteogenic differentiation RTPCR

BM-MSC were seeded on SiN, MTi, ATi and Zr discs in a 24-well plate at 40,000 cells/well. After cells became confluent, cells were treated with the osteogenic medium (StemPro®

Osteogenesis Differentiation kit (Thermo Fisher Scientific)). The culture medium was replaced twice a week. Total RNA was extracted from cultured BM-MSC on experimental 7 days and 14 days using the RNeasy kit (Qiagen, USA), and were then analyzed for quality and concentration using NanoDrop (Thermo Fisher Scientific). cDNA synthesis was carried out using the High-Capacity RNA-to-cDNA™ kit (Thermo Fisher Scientific) following the manufacturer's protocol. Quantitative real-time PCR (qPCR) was carried out using TaqMan primer/probe sets (Thermo Fisher Scientific), as per manufacturer instructions, for genes Runx family transcription factor 2 (RUNX2: Hs01047973_m1), alkaline phosphate (ALP: Hs01029142_m1), osteopontin (OPN: Hs00959010_m1), alpha 1 type I collagen (COL1A1: Hs00164004_m1) and osteocalcin (OCN: Hs01587814_g1).

4.5. RNA sequencing, bioinformatic analysis and validation RTPCR

Total RNA samples of BM-MSC cultured on SiN, MTi and ATi discs for 21 days were extracted using Quick RNA Miniprep kit (Zymo Research, Inc. Irvine, CA). Total RNA samples from 3 separate wells in the group were combined at the equal quantity. Libraries for RNA-Seq were prepared with KAPA Stranded mRNA-Seq Kit. The workflow consists of mRNA enrichment and fragmentation, first strand cDNA synthesis using random priming followed by second strand synthesis converting cDNA:RNA hybrid to double-stranded cDNA (dscDNA), and incorporates dUTP into the second cDNA strand. cDNA generation is followed by end repair to generate blunt ends, A-tailing, adaptor ligation and PCR amplification. Different adaptors were used for multiplexing samples in one lane. Sequencing was performed on Illumina Novaseq 6000 for PE 2x50 run. Data quality check was done on Illumina SAV. Demultiplexing was performed with Illumina Bcl2fastq v2.19.1.403 software and subjected to RNA sequencing (Illumina NextSeq 500, Illumina, Inc. San Diego, CA, USA). The sequence data were analyzed usUSing the RaNA-seq cloud platform.

Then, low-quality reads were removed, the data were aligned to the human genome GCHr38 and differential expression was done using the RaNA-seq cloud platform [54]. The Ensembl Transcripts release GRCm38.107 GTF was used for gene feature annotation. For normalization of transcripts counts, CPM normalized counts were generated by adding 1.0E-4 followed by counts per million (CPM) normalization. Differential Gene expression was determined by Partek Flow GSA algorithm (Partek® Flow® software, version 7.0 Copyright ©; 2019 Partek Inc., St. Louis, MO, USA). Gene ontology enrichment analysis for differentially expressed genes were performed using ShinyGo 0.77 [55]. The processed data were then further analyzed for gene ontogeny for biological pathway (BP), molecular function (MF) and cellular components (CC) as well as KEGG pathways by the use of gProfiler2 [56].

The expression of glutamate-ammonia ligase (GLUL: Hs00365928_g1) and hypoxia-inducible factor 1a (HIF1a: Hs00153153_m1) genes was determined by RTPCR as described above.

4.6. Mouse femur implant surgery and push-in test

Male 12-week-old C57Bl/6 mice (Strain # 000664; RRID: IMSR_JAX:000664; The Jackson Laboratory, Bar Harbor, ME, USUSA) were used. Animal was anesthetized by isoflurane inhalation and the distal femur was exposed. The implant site was prepared by disposable 25-gauge, and 23-gauge needles with a rubber stopper placed at 6 mm, and a miniature implant was press fitted retrogradely, followed by the skin closure [27]. Carprofen analgesics (5.0 mg/Kg) (Rimadyl, Zoetis USUS, Parsippany, NJ) was administered subcutaneously at the time of surgery and every 24 hours for 2 days after surgery.

At 1 week and 3 weeks of healing time mice were euthanized. The implant-containing femurs were harvested and immediately embedded on test table. The push-in test was performed using a custom-made stainless steel pushing rod mounted on a 1 kN load cell

(Instron, Canton, MA) and the push-in value was determined following the previously described protocol [19].

4.7. Micro-CT and bone morphometry

After the push-in test, mouse femurs were recovered and fixed in 10% buffered formalin and applied to micro-CT imaging (SkyScan 1275, Bruker, Billerica, MA, USA) at source voltage of 60 kV and source current of 166 μA with the scanning resolution of 10 μm per pixel. The region of interest for peri-implant bone was defined as 100μm periphery from the surface along the half of implant (3 mm long) in the bone marrow. The bone morphometric analysis was accomplished by CTAn software (Bruker).

4.8. Femur bone histology

After micro-CT imaging, mouse femurs were decalcified by 10% EDTA (Sigma-Aldrich) for 3-4 weeks and longitudinally hemisected along the implant. After the exposed implant was removed, femur samples were processed for paraffin-embedded sections (4 μm) with hematoxylin and eosin staining.

Photomicrographs were used to measure the bone-to-implant contact rate (BIC) using the previously reported method [19]. Furthermore, the thickness of the peri-implant bone was measured using a Java-based image processing program (ImageJ, National Institute of Health, Bethesda, MD, USA).

4.9. Immunohistochemistry

The femur sections were used for immunohistochemistry. The deparaffinized sections were subjected to a heat-induced epitope recovery treatment and incubated with primary monoclonal antibodies to CD31 (WM59, Cat# MA1-26196, ThermoFisher Scientific) and VEGFR3 (AFL4, Cat# 14-5988-82, ThermoFisher Scientific) at the suggested dilution followed by secondary

antibody incubation, diaminobenzidine staining and methylene blue counterstaining. Using VEGFR3 immunohistochemistry photomicrographs, the number of VEGFR3-positive vascular structure was counted.

4.10. Statistics

One-way analysis of variance (ANOVA) with post-hoc Tukey-Kramer formula was used to assess differences among multiple experimental groups; $p<0.05$ was considered to be statistically significant.

Acknowledgement

We thank Dr. Christopher Hamad, Department of Orthopaedic Surgery, UCLA David Geffen School of Medicine for providing his guidance on mouse implant surgery; UCLA Technology Center for Genomics & Bioinformatics for RNA sequencing; and Dr. Yunfeng Li, Translational Pathology Core Laboratory, UCLA David Geffen School of Medicine for immunohistochemistry work. This study was supported by a research fund and in-kind materials from SINTX Technologies, Salt Lake City, UT. TK was supported by JSPS Research Fellowship for Young Scientists (19J117670), SA was supported by the Watanabe Foundation certifies that the scholarship grant Grant Number WS2022-015 and Hiroo and Yukiko NAKATANI Graduate School of Medicine Scholarship Fund 2022. KEK-U was supported by the UCLA QCBio Collaboratory Fellowship awarded by the UCLA Institute for Quantitative & Computational Biosciences (QCB) 2019 – 2024.

Competing Interest

IN received a research fund and in-kind materials supported this study from SINTX Technologies, Salt Lake City, UT. IN is a consultant of FUJIFILM Corp, BioVinc LLC, and

Maruho Co. Ltd. AH is a consultant of Maruho Co. Ltd. BM and RB are employees of SINTX Technologies, Salt Lake City, UT. The other authors declare that no competing interests exist.

Data Availability

All data generated and analyzed during this study are included in the manuscript. Data will be made available on request. RNA sequencing data will be provided in NIH Gene Expression Omnibus at the time of publication.

Author Contributions

IN: designed the project.

BM, RB: developed the experimental materials.

WG, RK, TO: developed and characterized the experimental materials.

RB, GP: characterized the experimental materials.

WG, RK, IN, AH: performed *in vivo* studies.

TK, SA, TI: performed *in vitro* studies.

IF, AM: isolated human PDL-MSC.

IN, KEK-U: analyzed RNA sequencing data.

IN, AH: supervised the studies.

IN: drafted the initial manuscript.

GP: contributed manuscript and figures.

All authors: contributed to manuscript review

Table 1. Mechanical properties of silicon nitride (Si_3N_4: SiN), commercially pure titanium (Ti) and zirconia (Zr)

Property	SiN		Ti		Zr		Units (S.I.)
	Min	Max	Min	Max	Min	Max	
Atomic Volume (average)	0.0058	0.006	0.01	0.011	0.02	0.021	m3/kmol
Density	2.37	3.25	4.505	4.515	5	6.15	Mg/m3
Energy Content	150	200	750	1250	200	300	MJ/kg
Bulk Modulus	120	241	111	135	72.3	212	GPa
Compressive Strength	524	5500	130	170	1200	5200	MPa
Ductility	0.00031	0.00169	0.25	0.4	0.00066	0.0035	
Elastic Limit	60	525	172	240	115	711	MPa
Endurance Limit	44	470	176	223	107	640	MPa
Fracture Toughness	1.8	6.5	55	60	1	8	MPa.m1/2
Hardness	8000	305000	1150	1250	5500	15750	MPa
Loss Coefficient	2.00E-05	5.00E-05	0.002	0.003	0.0005	0.001	
Modulus of Rupture	181	1050	130	170	177	1000	MPa
Poisson's Ratio	0.23	0.28	0.35	0.37	0.22	0.32	
Shear Modulus	65.3	127	36	39	53.4	86.4	GPa
Tensile Strength	60	525	240	360	115	711	MPa
Young's Modulus	166	297	100	105	100	250	GPa

References

[1] L.K. George, D. Ruiz, Jr., F.A. Sloan, The effects of total hip arthroplasty on physical functioning in the older population, J Am Geriatr Soc 56(6) (2008) 1057-62.
[2] H. Bang, Y.L. Chiu, S.G. Memtsoudis, L.A. Mandl, A.G. Della Valle, A.I. Mushlin, R.G. Marx, M. Mazumdar, Total hip and total knee arthroplasties: trends and disparities revisited, Am J Orthop (Belle Mead NJ) 39(9) (2010) E95-102.
[3] P. Cram, X. Lu, S.L. Kates, J.A. Singh, Y. Li, B.R. Wolf, Total knee arthroplasty volume, utilization, and outcomes among Medicare beneficiaries, 1991-2010, JAMA 308(12) (2012) 1227-36.
[4] C. Bural, H. Bilhan, A. Cilingir, O. Geckili, Assessment of demographic and clinical data related to dental implants in a group of Turkish patients treated at a university clinic, J Adv Prosthodont 5(3) (2013) 351-8.
[5] D. Apostu, O. Lucaciu, C. Berce, D. Lucaciu, D. Cosma, Current methods of preventing aseptic loosening and improving osseointegration of titanium implants in cementless total hip arthroplasty: a review, J Int Med Res 46(6) (2018) 2104-2119.
[6] D.D. Bosshardt, V. Chappuis, D. Buser, Osseointegration of titanium, titanium alloy and zirconia dental implants: current knowledge and open questions, Periodontol 2000 73(1) (2017) 22-40.
[7] T. Ogawa, Ultraviolet photofunctionalization of titanium implants, Int J Oral Maxillofac Implants 29(1) (2014) e95-102.
[8] J.C.M. Souza, M.B. Sordi, M. Kanazawa, S. Ravindran, B. Henriques, F.S. Silva, C. Aparicio, L.F. Cooper, Nano-scale modification of titanium implant surfaces to enhance osseointegration, Acta Biomater 94 (2019) 112-131.
[9] T. Hanawa, Zirconia versus titanium in dentistry: A review, Dent Mater J 39(1) (2020) 24-36.
[10] F.H. Schunemann, M.E. Galarraga-Vinueza, R. Magini, M. Fredel, F. Silva, J.C.M. Souza, Y. Zhang, B. Henriques, Zirconia surface modifications for implant dentistry, Mater Sci Eng C Mater Biol Appl 98 (2019) 1294-1305.
[11] X. Du, S.S. Lee, G. Blugan, S.J. Ferguson, Silicon Nitride as a Biomedical Material: An Overview, Int J Mol Sci 23(12) (2022).
[12] N. Ahuja, K.R. Awad, M. Brotto, P.B. Aswath, V. Varanasi, A comparative study on silicon nitride, titanium and polyether ether ketone on mouse pre-osteoblast cells, Med Devices Sens 4(1) (2021).
[13] Y. Shen, K. Fang, Y. Xiang, K. Xu, L. Yu, J. Chen, P. Ma, K. Cai, X. Shen, J. Liu, Improvement in osteogenesis, vascularization, and corrosion resistance of titanium with silicon-nitride doped micro-arc oxidation coatings, Front Bioeng Biotechnol 10 (2022) 1023032.
[14] H. Wu, L. Yang, J. Qian, D. Wang, Y. Pan, X. Wang, S. Nabanita, T. Tang, J. Zhao, J. Wei, Microporous Coatings of PEKK/SN Composites Integration with PEKK Exhibiting Antibacterial and Osteogenic Activity, and Promotion of Osseointegration for Bone Substitutes, ACS Biomater Sci Eng 5(3) (2019) 1290-1301.
[15] F. Boschetto, E. Marin, E. Ohgitani, T. Adachi, M. Zanocco, S. Horiguchi, W. Zhu, B.J. McEntire, O. Mazda, B.S. Bal, G. Pezzotti, Surface functionalization of PEEK with silicon nitride, Biomed Mater 16(1) (2020).
[16] Y. Dai, L. Chu, Z. Luo, T. Tang, H. Wu, F. Wang, S. Mei, J. Wei, X. Wang, X. Shang, Effects of a Coating of Nano Silicon Nitride on Porous Polyetheretherketone on Behaviors of MC3T3-E1 Cells in Vitro and Vascularization and Osteogenesis in Vivo, ACS Biomater Sci Eng 5(12) (2019) 6425-6435.

[17] C.M. Mengatto, F. Mussano, Y. Honda, C.S. Colwell, I. Nishimura, Circadian rhythm and cartilage extracellular matrix genes in osseointegration: a genome-wide screening of implant failure by vitamin D deficiency, PLoS One 6(1) (2011) e15848.
[18] N. Hassan, K. McCarville, K. Morinaga, C.M. Mengatto, P. Langfelder, A. Hokugo, Y. Tahara, C.S. Colwell, I. Nishimura, Titanium biomaterials with complex surfaces induced aberrant peripheral circadian rhythms in bone marrow mesenchymal stromal cells, PLoS One 12(8) (2017) e0183359.
[19] K. Morinaga, H. Sasaki, S. Park, A. Hokugo, H. Okawa, Y. Tahara, C.S. Colwell, I. Nishimura, Neuronal PAS domain 2 (Npas2) facilitated osseointegration of titanium implant with rough surface through a neuroskeletal mechanism, Biomaterials 192 (2019) 62-74.
[20] G. Pezzotti, Silicon Nitride: A Bioceramic with a Gift, ACS Appl Mater Interfaces 11(30) (2019) 26619-26636.
[21] G. Pezzotti, E. Marin, T. Adachi, A. Rondinella, F. Boschetto, W. Zhu, N. Sugano, R.M. Bock, B. McEntire, S.B. Bal, Bioactive silicon nitride: A new therapeutic material for osteoarthropathy, Sci Rep 7 (2017) 44848.
[22] M. Zanocco, E. Marin, A. Rondinella, F. Boschetto, S. Horiguchi, W. Zhu, B.J. McEntire, R.M. Bock, B.S. Bal, G. Pezzotti, The role of nitrogen off-stoichiometry in the osteogenic behavior of silicon nitride bioceramics, Mater Sci Eng C Mater Biol Appl 105 (2019) 110053.
[23] J. Fan, J.J. Kamphorst, R. Mathew, M.K. Chung, E. White, T. Shlomi, J.D. Rabinowitz, Glutamine-driven oxidative phosphorylation is a major ATP source in transformed mammalian cells in both normoxia and hypoxia, Mol Syst Biol 9 (2013) 712.
[24] S. Vidali, S. Aminzadeh, B. Lambert, T. Rutherford, W. Sperl, B. Kofler, R.G. Feichtinger, Mitochondria: The ketogenic diet--A metabolism-based therapy, Int J Biochem Cell Biol 63 (2015) 55-9.
[25] M. Chiu, D. Toscani, V. Marchica, G. Taurino, F. Costa, M.G. Bianchi, R. Andreoli, V. Franceschi, P. Storti, J. Burroughs-Garcia, R.A. Eufemiese, B. Dalla Palma, N. Campanini, E. Martella, C. Mancini, J. Shan, M.S. Kilberg, G. D'Amico, E. Dander, L. Agnelli, G. Pruneri, G. Donofrio, O. Bussolati, N. Giuliani, Myeloma Cells Deplete Bone Marrow Glutamine and Inhibit Osteoblast Differentiation Limiting Asparagine Availability, Cancers (Basel) 12(11) (2020).
[26] H.N. Kung, J.R. Marks, J.T. Chi, Glutamine synthetase is a genetic determinant of cell type-specific glutamine independence in breast epithelia, PLoS Genet 7(8) (2011) e1002229.
[27] W. Xi, V. Hegde, S.D. Zoller, H.Y. Park, C.M. Hart, T. Kondo, C.D. Hamad, Y. Hu, A.H. Loftin, D.O. Johansen, Z. Burke, S. Clarkson, C. Ishmael, K. Hori, Z. Mamouei, H. Okawa, I. Nishimura, N.M. Bernthal, T. Segura, Point-of-care antimicrobial coating protects orthopaedic implants from bacterial challenge, Nat Commun 12(1) (2021) 5473.
[28] T. Albrektsson, C. Johansson, Osteoinduction, osteoconduction and osseointegration, Eur Spine J 10 Suppl 2(Suppl 2) (2001) S96-101.
[29] I. Nishimura, Genetic networks in osseointegration, J Dent Res 92(12 Suppl) (2013) 109S-18S.
[30] K. Komatsu, T. Matsuura, T. Suzumura, T. Ogawa, Genome-wide transcriptional responses of osteoblasts to different titanium surface topographies, Mater Today Bio 23 (2023) 100852.
[31] E. Sabini, L. Arboit, M.P. Khan, G. Lanzolla, E. Schipani, Oxidative phosphorylation in bone cells, Bone Rep 18 (2023) 101688.
[32] R. Sautchuk, Jr., R.A. Eliseev, Cell energy metabolism and bone formation, Bone Rep 16 (2022) 101594.

[33] C. Lin, Q. Yang, D. Guo, J. Xie, Y.S. Yang, S. Chaugule, N. DeSouza, W.T. Oh, R. Li, Z. Chen, A.A. John, Q. Qiu, L.J. Zhu, M.B. Greenblatt, S. Ghosh, S. Li, G. Gao, C. Haynes, C.P. Emerson, J.H. Shim, Impaired mitochondrial oxidative metabolism in skeletal progenitor cells leads to musculoskeletal disintegration, Nat Commun 13(1) (2022) 6869.
[34] L.C. Shum, A.M. Hollenberg, A.L. Baldwin, B.H. Kalicharan, N. Maqsoodi, P.T. Rubery, A. Mesfin, R.A. Eliseev, Role of oxidative metabolism in osseointegration during spinal fusion, PLoS One 15(11) (2020) e0241998.
[35] X. Zhang, J. Sun, M. Zhou, C. Li, Z. Zhu, X. Gan, The role of mitochondria in the peri-implant microenvironment, Exp Physiol 108(3) (2023) 398-411.
[36] Y. Liu, X. Zhang, W. Wang, T. Liu, J. Ren, S. Chen, T. Lu, Y. Tie, X. Yuan, F. Mo, J. Yang, Y. Wei, X. Wei, Ammonia promotes the proliferation of bone marrow-derived mesenchymal stem cells by regulating the Akt/mTOR/S6k pathway, Bone Res 10(1) (2022) 57.
[37] H.C. Yoo, Y.C. Yu, Y. Sung, J.M. Han, Glutamine reliance in cell metabolism, Exp Mol Med 52(9) (2020) 1496-1516.
[38] R. Bornstein, M.T. Mulholland, M. Sedensky, P. Morgan, S.C. Johnson, Glutamine metabolism in diseases associated with mitochondrial dysfunction, Mol Cell Neurosci 126 (2023) 103887.
[39] F. Diomede, G.D. Marconi, L. Fonticoli, J. Pizzicanella, I. Merciaro, P. Bramanti, E. Mazzon, O. Trubiani, Functional Relationship between Osteogenesis and Angiogenesis in Tissue Regeneration, Int J Mol Sci 21(9) (2020).
[40] S.M. Anderson, S.N. Siegman, T. Segura, The effect of vascular endothelial growth factor (VEGF) presentation within fibrin matrices on endothelial cell branching, Biomaterials 32(30) (2011) 7432-43.
[41] C.H. Dreyer, K. Kjaergaard, M. Ding, L. Qin, Vascular endothelial growth factor for in vivo bone formation: A systematic review, J Orthop Translat 24 (2020) 46-57.
[42] V.B. Kumar, O.S. Tiwari, G. Finkelstein-Zuta, S. Rencus-Lazar, E. Gazit, Design of Functional RGD Peptide-Based Biomaterials for Tissue Engineering, Pharmaceutics 15(2) (2023).
[43] A. Okamura, T. Hiratsuka, H. Fushimi, I. Nishimura, Recombinant bone matrix maintains the graft space, induces vascularized bone regeneration and preserves canine tooth extraction socket structure, J Clin Periodontol 51(3) (2024) 338-353.
[44] T. Hiratsuka, I. Ogura, A. Okamura, H. Fushimi, K. Yamaguchi, I. Nishimura, Bioresorbable Bone Graft Composed of an RGD-Enriched Recombinant Human Collagen Polypeptide Induced Neovascularization and Regeneration of Mature Bone Tissue, ACS Appl Bio Mater 3(12) (2020) 8592-8602.
[45] F.A.D. Monte, K.R. Awad, N. Ahuja, H.K.W. Kim, P. Aswath, M. Brotto, V.G. Varanasi, Amorphous Silicon Oxynitrophosphide-Coated Implants Boost Angiogenic Activity of Endothelial Cells, Tissue Eng Part A 26(1-2) (2020) 15-27.
[46] L.A. Ridnour, J.S. Isenberg, M.G. Espey, D.D. Thomas, D.D. Roberts, D.A. Wink, Nitric oxide regulates angiogenesis through a functional switch involving thrombospondin-1, Proc Natl Acad Sci U S A 102(37) (2005) 13147-52.
[47] J.P. Cooke, D.W. Losordo, Nitric oxide and angiogenesis, Circulation 105(18) (2002) 2133-5.
[48] L. Mosteo, J. Storer, K. Batta, E.J. Searle, D. Duarte, D.H. Wiseman, The Dynamic Interface Between the Bone Marrow Vascular Niche and Hematopoietic Stem Cells in Myeloid Malignancy, Front Cell Dev Biol 9 (2021) 635189.

[49] R.M. Monaghan, D.J. Page, P. Ostergaard, B.D. Keavney, The physiological and pathological functions of VEGFR3 in cardiac and lymphatic development and related diseases, Cardiovasc Res 117(8) (2021) 1877-1890.
[50] T. Tammela, G. Zarkada, E. Wallgard, A. Murtomaki, S. Suchting, M. Wirzenius, M. Waltari, M. Hellstrom, T. Schomber, R. Peltonen, C. Freitas, A. Duarte, H. Isoniemi, P. Laakkonen, G. Christofori, S. Yla-Herttuala, M. Shibuya, B. Pytowski, A. Eichmann, C. Betsholtz, K. Alitalo, Blocking VEGFR-3 suppresses angiogenic sprouting and vascular network formation, Nature 454(7204) (2008) 656-60.
[51] A. Lin, C.J. Wang, J. Kelly, P. Gubbi, I. Nishimura, The role of titanium implant surface modification with hydroxyapatite nanoparticles in progressive early bone-implant fixation in vivo, Int J Oral Maxillofac Implants 24(5) (2009) 808-16.
[52] R.M. Bock, B.J. McEntire, B.S. Bal, M.N. Rahaman, M. Boffelli, G. Pezzotti, Surface modulation of silicon nitride ceramics for orthopaedic applications, Acta Biomater 26 (2015) 318-30.
[53] M. Ishijima, A. Ghassemi, P. Soltanzadeh, M. Tanaka, K. Nakhaei, W. Park, M. Hirota, N. Tsukimura, T. Ogawa, Effect of UV Photofunctionalization on Osseointegration in Aged Rats, Implant Dent 25(6) (2016) 744-750.
[54] C. Prieto, D. Barrios, RaNA-Seq: Interactive RNA-Seq analysis from FASTQ files to functional analysis, Bioinformatics (2019).
[55] S.X. Ge, D. Jung, R. Yao, ShinyGO: a graphical gene-set enrichment tool for animals and plants, Bioinformatics 36(8) (2020) 2628-2629.
[56] U. Raudvere, L. Kolberg, I. Kuzmin, T. Arak, P. Adler, H. Peterson, J. Vilo, g:Profiler: a web server for functional enrichment analysis and conversions of gene lists (2019 update), Nucleic Acids Res 47(W1) (2019) W191-W198.

Figure 1 Characterization of Silicon Nitride (SiN), Machined and Acid-etched Titanium (MTi, ATi) and Zirconia (Zr) materials.

A. Discs (12.7 mm diameter, 1 mm thick) were generated for *in vitro* study using SiN (Si_3N_4), MTi, ATi and Zr. **B.** SEM surface characterization revealed the nanocrystalline structure of SiN and Zr ceramic materials. MTi and ATi materials showed anisotropic and isotropic surface structures, respectively. **C**. Surface topography characterization demonstrated micro-rough surface of ATi material (n=6 per group). **D**. The wettability test revealed that all materials were in the hydrophilic range. (n=6 per group). **E**. Human BM-MSC cultured on the materials were spread with developed cytoskeleton. No differences were observed.

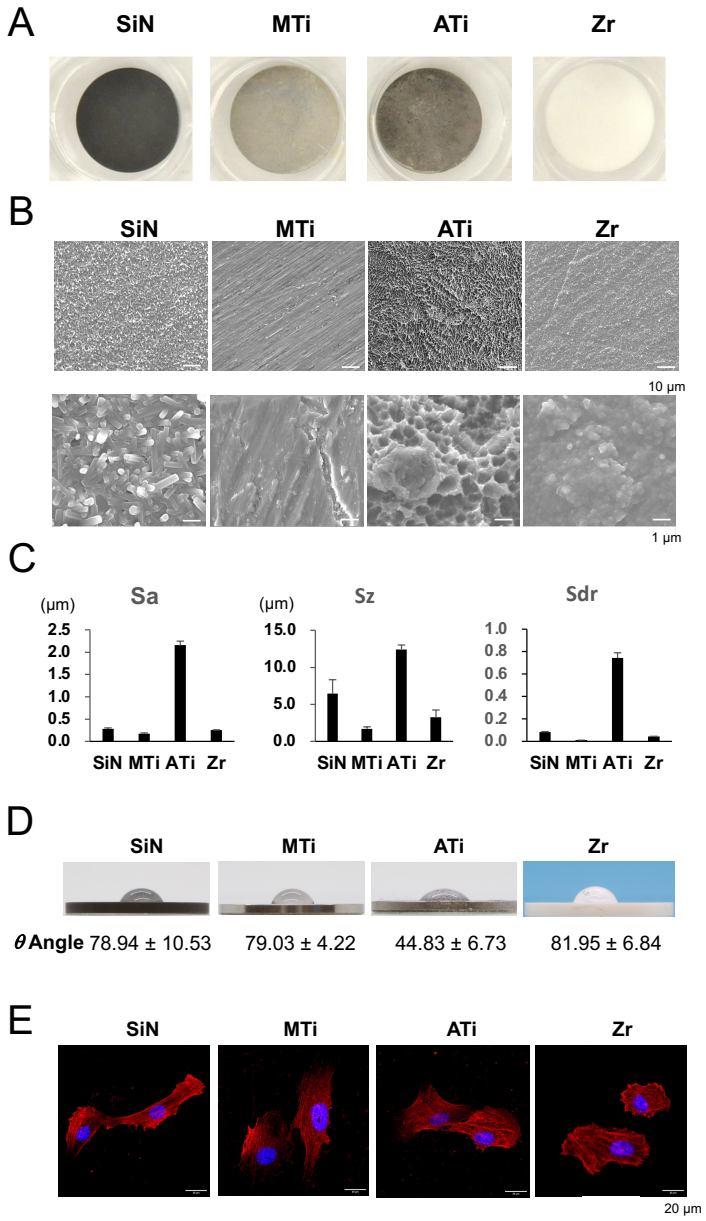

Figure 2. Behaviors of BM-MSC exposed to SiN, MTi, ATi and Zr discs.

A. Wst-1 assay demonstrated that these materials did not affect the cell viability and proliferation of BM-MSC (n=3 per group). **B**. *In vitro* mineralization measured by alizarin red S staining increased in the SiN group (n=4 per group). **C**. RTPCR analysis (n=3~4 per group) did not identify the effect of materials on the expression of osteogenic differentiation-related genes. However, a core circadian rhythm gene, NPAS2, was upregulated by SiN and ATi as compared to MTi, albeit the statistical significance was reached only between SiN and MTi.

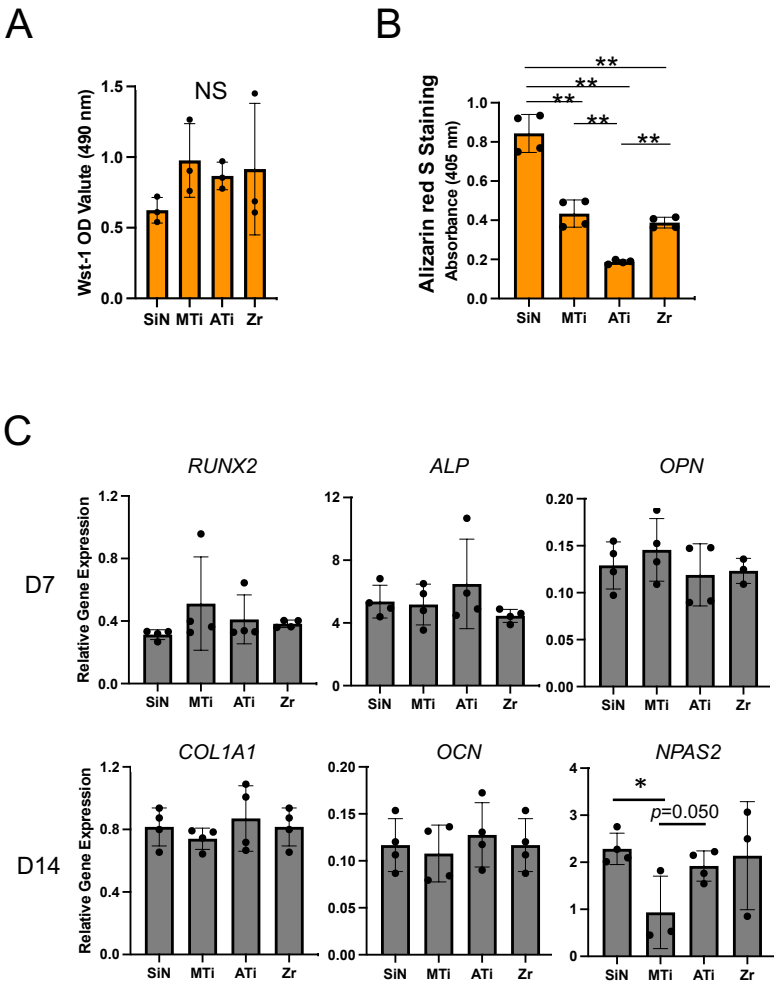

Figure 3. RNA sequencing data analysis revealed enrichment of mitochondria oxidative phosphorylation by SiN.

A. Molecular Function and Cellular Component gene ontogeny as well as KEGG pathway analyses depicted that the functional enrichment of mitochondrial oxidative phosphorylation pathways in BM-MSC exposed to SiN. **B**. Hypothetical diagram of ammonium/ammonia released from SiN material, which may be integrated in the glutamine-driven mitochondrial oxidative phosphorylation. In addition, SiN-derived ammonia is thought to processed to generate nitric oxide (NO). **C**. Chemical diagram processing glutamate to glutamine by glutamine-ammonia ligase (GLUL). **D**. RTPCR revealed the upregulation of *GLUL* by osteogenic media but it was not influenced by biomaterials.

A

Molecular Function	Fold Enrichment		nGenes		Enrichment FDR	
	SiN v Mti	SiN v Ati	SiN v Mti	SiN v Ati	SiN v Mti	SiN v Ati
NADH dehydrogenase (quinone) activity	23.36	9.27	7	6	8.80E-07	1.01E-03
NADH dehydrogenase activity	22.98	9.12	7	6	8.98E-07	1.04E-03
NAD(P)H dehydrogenase (quinone) activity	22.26	8.83	7	6	1.03E-06	1.21E-03
NADH dehydrogenase (ubiquinone) activity	20.35	7.85	6	5	1.22E-05	6.38E-03
Oxidoreductase activity, acting on NAD(P)H, quinone or similar compound as acceptor	18.50	7.34	7	6	3.25E-06	2.97E-03
Oxidoreduction-driven active transmembrane transporter activity	18.32	9.42	9	10	9.89E-08	5.53E-06
Oxidoreductase activity, acting on NAD(P)H	13.07	5.19	7	6	2.41E-05	1.28E-02
Electron transfer activity	11.59	6.56	9	11	2.96E-06	3.41E-05
Oxidoreductase activity	4.14	2.82	17	25	1.56E-05	9.41E-05
KEGG	**Fold Enrichment**		**nGenes**		**Enrichment FDR**	
	SiN v Mti	SiN v Ati	SiN v Mti	SiN v Ati	SiN v Mti	SiN v Ati
Oxidative phosphorylation	16.71	7.73	11	11	2.35E-09	3.38E-06
Thermogenesis	10.53	5.68	12	14	2.59E-08	3.38E-06
Cellular Component	**Fold Enrichment**		**nGenes**		**Enrichment FDR**	
	SiN v Mti	SiN v Ati	SiN v Mti	SiN v Ati	SiN v Mti	SiN v Ati
Respirasome	15.66	7.25	9	9	2.38E-07	4.69E-05
Mitochondrial respirasome	15.96	6.46	8	7	1.34E-06	8.10E-04
Respiratory chain complex	18.14	8.39	9	9	7.84E-08	1.50E-05
Mitochondrial respiratory chain complex I	18.50	7.14	6	5	1.56E-05	4.20E-03
Oxidoreductase complex	12.34	6.42	8	9	7.05E-06	1.15E-04
NADH dehydrogenase complex	18.50	7.14	6	5	1.56E-05	4.20E-03

B

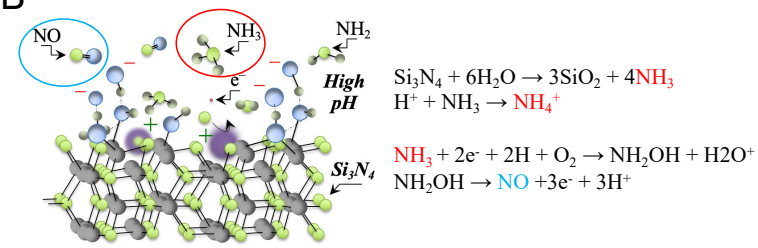

C

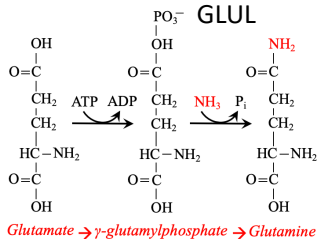

D

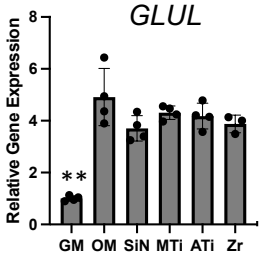

Figure 4. Osseointegration analysis of SiN, MTi and ATi miniature implants in mouse femur.

A. Miniature implants were fabricated for mouse femur. **B**. Surgical placement of miniature implant to mouse femur. **C**. Implant push-in test. The push-in value was determined at the break point of bone and implant bonding. **D**. The implant push-in value at 1 week (n=4 per group) and 3 weeks (n=6 per group) of healing time.

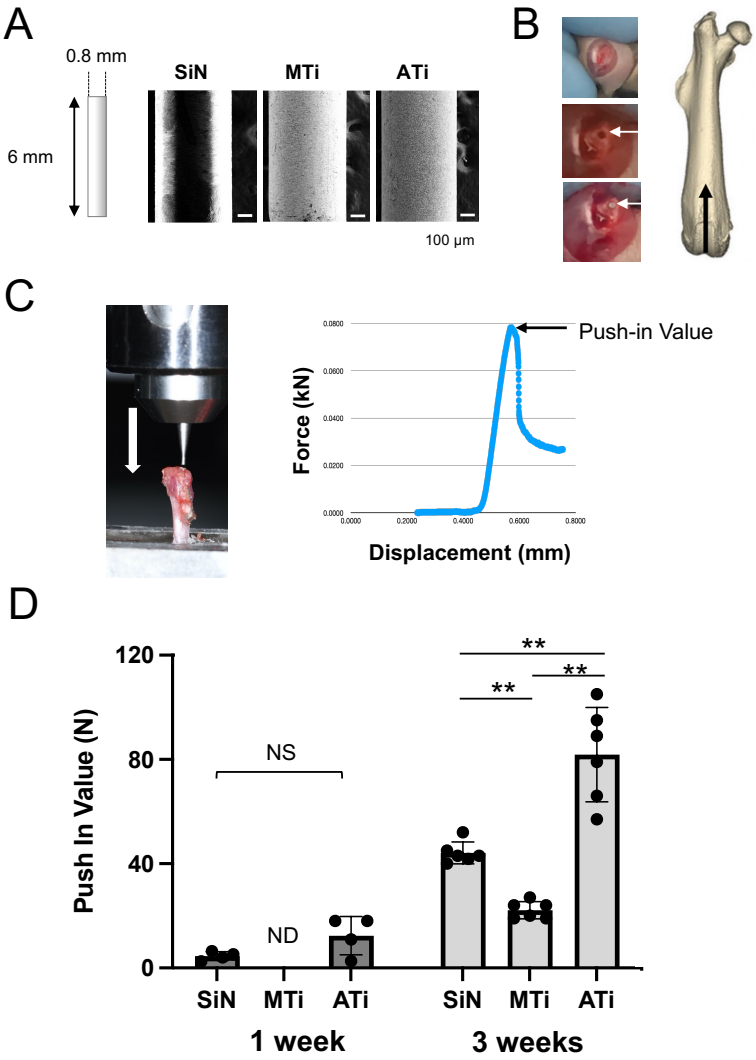

Figure 5. Micro-CT bone morphometry of peri-implant bone

A. A longitudinal section and a cross section micro-CT images depicting the peri-implant bone region of interest (ROI). SiN implant was radiolucent. **B**. Peri-implant bone morphometric measurement (n=6 per group). Significant increase in the SiN peri-implant bone was suggested.

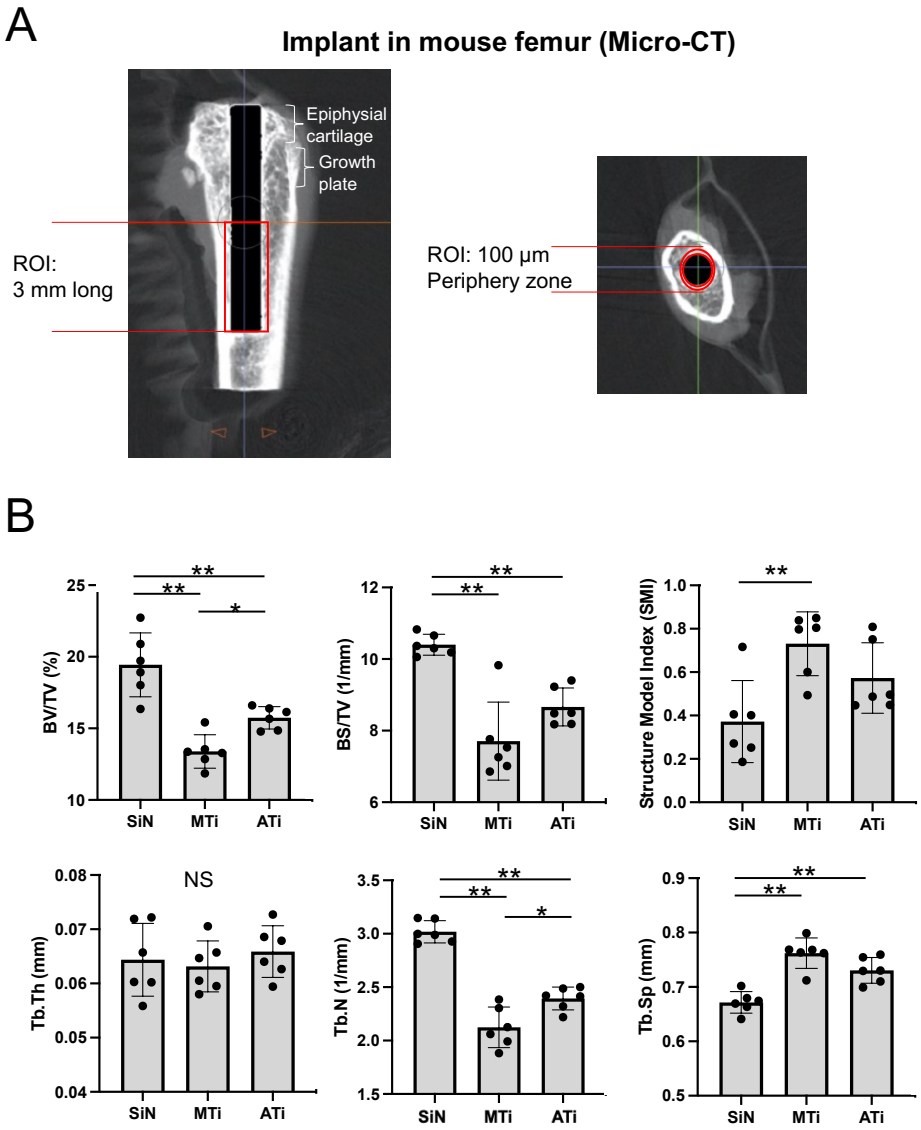

Figure 6. Histological evaluation of peri-implant bone

A. Peri-implant bone (pI Bone) associated with SiN implant was thick and well adopted. By contrast, peri-implant bone of MTi was thin and small and of ATi was fragmented. The bone marrow around MTi implant showed increased adipose tissue (Ap). **B**. High magnification view showed periodic connective tissue fibers (arrows) extended in the bone-to-implant contact (BIC) of SiN implant. There was a layer of cells between the peri-implant bone and MTi implant. **C**. BIC rate of SiN Implant and ATi implant was larger than MTi implant (n=5 per group). **D**. SiN associated peri-implant bone was thicker (wider) than those of MTi and ATi implants (10 measurement sites per group).

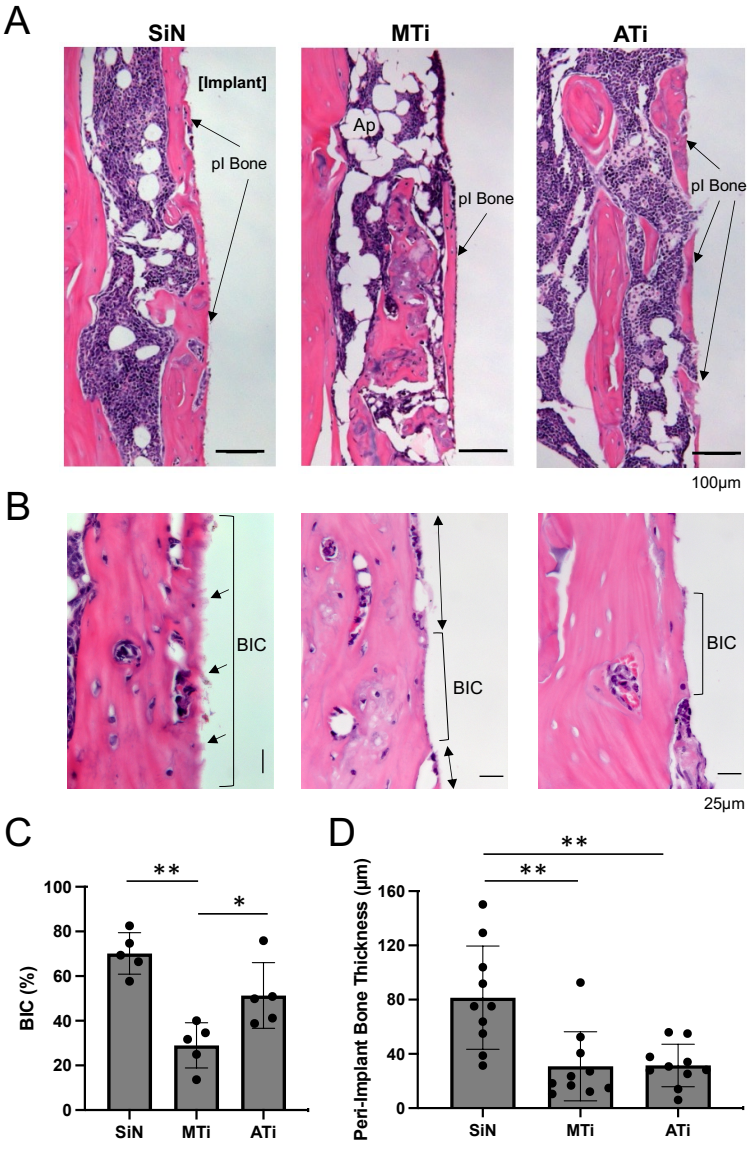

Figure 7. RNA sequencing data analysis by Biological Pathway

A. The top 20 Biological Pathway gene ontogeny included the increased gene clusters related to vascular formation (green shade) in the SiN group. **B**. The validation RTPCR demonstrated the increased steady state expression of the key gene, HIF1a in the SiN group.

A

	Enrichment FDR	nGenes	Fold Enrichment	Biological Pathway
SiN v MTi	4.97E-20	28	12.66	Extracellular matrix organization
	4.97E-20	28	12.64	Extracellular structure organization
	4.97E-20	28	12.55	External encapsulating structure organization
	1.34E-10	18	9.62	Cell-substrate adhesion
	2.56E-09	16	9.41	ATP metabolic process
	4.43E-13	25	8.01	**Blood vessel morphogenesis**
	6.89E-11	21	7.86	**Angiogenesis**
	4.77E-12	25	7.10	**Blood vessel development**
	1.64E-12	26	7.07	**Vasculature development**
	1.64E-10	23	6.52	Response to wounding
	4.26E-11	26	5.97	**Tube morphogenesis**
	2.36E-11	29	5.40	**Tube development**
	3.88E-11	29	5.26	Enzyme linked receptor protein signaling pathway
	3.88E-11	29	5.24	**Circulatory system development**
	4.60E-09	24	5.16	Regulation of cell migration
	1.48E-10	33	4.22	Cell migration
	2.96E-10	33	4.10	Cell adhesion
	3.12E-10	33	4.08	Biological adhesion
	4.18E-10	34	3.90	Cell motility
	4.18E-10	34	3.90	Localization of cell
SiN v ATi	2.42E-16	20	16.82	SRP-dependent cotranslational protein targeting to membrane
	4.41E-16	20	15.97	Cotranslational protein targeting to membrane
	2.22E-16	21	15.45	Protein targeting to ER
	5.27E-21	27	15.05	Cytoplasmic translation
	3.20E-16	21	14.99	Establishment of protein localization to endoplasmic reticulum
	1.77E-15	21	13.46	Nuclear-transcribed mRNA catabolic process, nonsense-mediated decay
	9.16E-16	22	12.79	Protein localization to endoplasmic reticulum
	5.69E-23	41	8.58	Extracellular matrix organization
	5.69E-23	41	8.56	Extracellular structure organization
	5.69E-23	41	8.51	External encapsulating structure organization
	5.14E-16	36	6.23	**Angiogenesis**
	7.03E-17	40	5.93	**Blood vessel morphogenesis**
	3.83E-16	41	5.39	**Blood vessel development**
	3.20E-16	42	5.29	**Vasculature development**
	2.42E-15	44	4.68	**Tube morphogenesis**
	3.66E-17	52	4.48	**Tube development**
	3.33E-16	51	4.26	**Circulatory system development**
	7.70E-16	51	4.15	Viral process
	2.44E-15	60	3.45	Cell adhesion
	2.84E-15	60	3.43	Biological adhesion

B

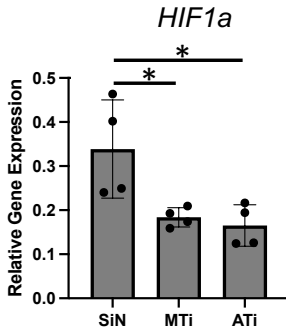

Figure 8. Increased CD31^{dim}VEGFR3^{+} vascular structures in bone marrow around SiN implant
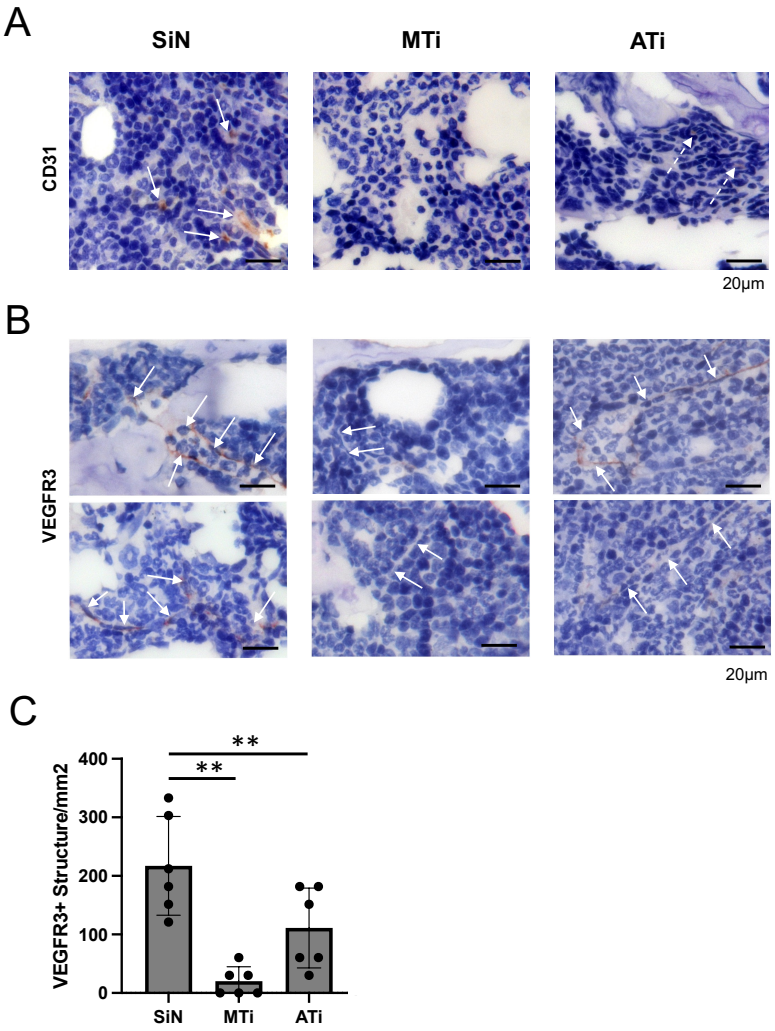
A. Immunohistochemistry with anti-CD31 antibody depicted faint staining (while arrows). **B**. Immunohistochemistry with anti-VEGFR3 showed strong staining of vascular-like structures in peri-implant bone marrow of SiN implant (white arrows). There were vascular-like structures in peri-implant bone marrow of MTi implant, which were negative with VEGFR3 staining (white arrows). In peri-implant bone marrow of ATi implant, there were VEGFR3 positive vascular-like structures (white arrows). **C**. The VEGFR3 positive vascular-like structure was found more densely in peri-implant bone marrow of SiN implant.